CHEMICAL PHYSICS

Ultrafast electron diffraction imaging of bond breaking in di-ionized acetylene

B. Wolter,[1]* M. G. Pullen,[1]* A.-T. Le,[2] M. Baudisch,[1] K. Doblhoff-Dier,[3] A. Senftleben,[4] M. Hemmer,[1,5] C. D. Schröter,[6] J. Ullrich,[6,7] T. Pfeifer,[6] R. Moshammer,[6] S. Gräfe,[8,9] O. Vendrell,[5,10] C. D. Lin,[2] J. Biegert[1,11]†

Visualizing chemical reactions as they occur requires atomic spatial and femtosecond temporal resolution. Here, we report imaging of the molecular structure of acetylene (C_2H_2) 9 femtoseconds after ionization. Using mid-infrared laser–induced electron diffraction (LIED), we obtained snapshots as a proton departs the $[C_2H_2]^{2+}$ ion. By introducing an additional laser field, we also demonstrate control over the ultrafast dissociation process and resolve different bond dynamics for molecules oriented parallel versus perpendicular to the LIED field. These measurements are in excellent agreement with a quantum chemical description of field-dressed molecular dynamics.

Ultrafast imaging of atomic motion in real time during transitions in molecular structure is a prerequisite to disentangling the complex interplay between reactants and products (*1*, *2*) because the movements of all atoms are coupled. Ultrafast absorption and emission spectroscopic techniques have uncovered numerous insights in chemical reaction dynamics (*3*, *4*) but are limited by their reliance on local chromophores and their associated ladders of quantum states rather than global structural characterization.

Reaction imaging at the molecular level requires a combination of few-femtosecond temporal and picometer spatial measurement resolution (*5*). Among the many techniques that are currently under intense development, x-ray scattering can reach few-femtosecond pulse durations at photon energies of 8.3 keV (1.5 Å) (*6*) with a demonstrated measurement resolution of 3.5 Å (*7*). Challenges for such photon-based approaches are the coarse spatial resolution and the low scattering cross sections, especially for gas-phase investigations. Electron scattering (*8*) provides much-larger-interaction cross sections and smaller de Broglie wavelengths but suffers from space charge broadening, which decreases the temporal resolution. Consequently, measurements have demonstrated 7-pm spatial and 100-fs temporal resolution (*9*, *10*) in gas-phase experiments. Remedies to improve temporal resolution include relativistic electron acceleration (*11*) or electron bunch compression (*12*) with 100- and 28-fs limits, respectively. Compared with such incoherent scattering of electrons from an electron source off a molecular target, laser-induced electron diffraction (LIED) is a self-imaging method based on coherent electron scattering (*13*–*17*). In LIED, one electron is liberated from the target molecule through tunnel ionization and then accelerated in the field and rescattered off its molecular ion, acquiring structural information. The electron recollision process occurs within one optical cycle of the laser field and permits the mapping of electron momenta to recollision time (*18*, *19*).

Here, we used LIED to image an entire hydrocarbon molecule [acetylene (C_2H_2)] at 9 fs after ionization-triggered dissociation and visualize the departure of a proton. Our methodology combined mid-infrared (mid-IR) LIED with single-molecule coincidence detection in a reaction microscope (*20*–*22*) and used an additional laser control field to impulsively align the molecule (supplementary materials). The laser control field, a 1700-nm pulse, was sent before the 3100-nm LIED pulse and oriented the rotationally cold C_2H_2 molecule parallel or perpendicular to the LIED field depending on the time delay. The 3100-nm pulse triggered molecular dissociation and, at the same time, collected structural snapshots of the entire C_2H_2 molecule. The alignment-dependent dynamics (*23*) were structurally imaged for both orientations. We chose C_2H_2 because it is one of the best-studied hydrocarbons (*24*–*27*) and offers the numerous degrees of freedom and multitude of structural dynamics found also in larger and more complex molecules (*1*, *28*, *29*). Because of the strong field nature of LIED, many different fragmentation channels and ionization states occur simultaneously. Our specific implementation of mid-IR LIED with single-molecule coincidence detection provides a remedy because post-selection of data regains channel selectivity.

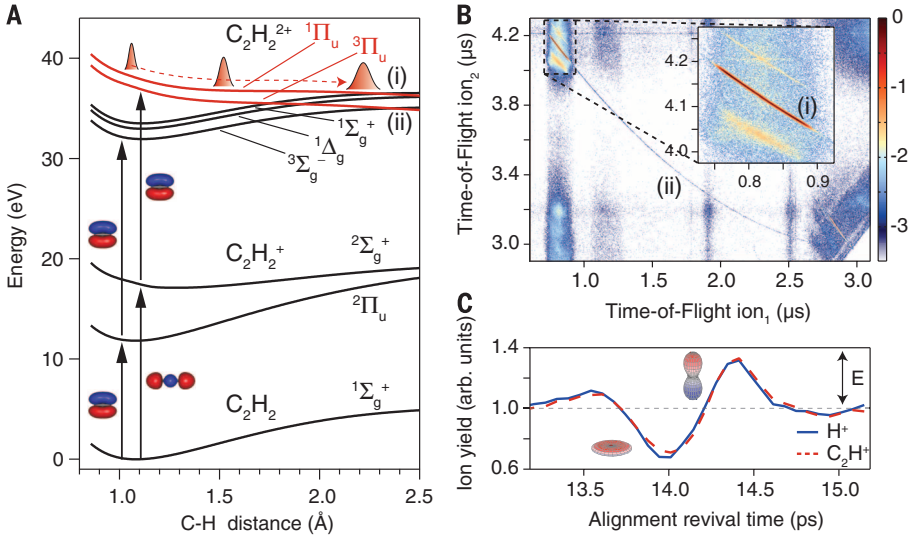

Fig. 1. Identification of the relevant states leading to proton ejection. (**A**) The calculated relevant energy levels and possible pathways (*34*) leading to dissociation of C_2H_2 and departure of one proton (*26*, *35*). The calculation is detailed in the supplementary materials. Two main pathways are identified, one leading to dissociative PES and fast dissociation (i), the other via metastable states to slow dissociation (ii). (**B**) These pathways are identified in the PIPICO analysis and (**C**) exhibit alignment-dependent fragment yields. (B) is shown here for perpendicularly oriented C_2H_2; the parallel case is provided in fig. S4.

[1]ICFO–Institut de Ciencies Fotoniques, The Barcelona Institute of Science and Technology, 08860 Castelldefels, Barcelona, Spain. [2]J. R. Macdonald Laboratory, Physics Department, Kansas State University, Manhattan, KS 66506-2604, USA. [3]Leiden Institute of Chemistry, Gorlaeus Laboratories, Leiden University, Post Office Box 9502, 2300 RA Leiden, Netherlands. [4]Universität Kassel, Institut für Physik und CINSaT, Heinrich-Plett-Str. 40, 34132 Kassel, Germany. [5]Center for Free-Electron Laser Science, Deutsches Elektronen-Synchrotron (DESY), Centre for Ultrafast Imaging (CUI), 22607 Hamburg, Germany. [6]Max-Planck-Institut für Kernphysik, Saupfercheckweg 1, 69117 Heidelberg, Germany. [7]Physikalisch-Technische Bundesanstalt (PTB), Bundesallee 100, 38116 Braunschweig, Germany. [8]Institute for Physical Chemistry, Friedrich-Schiller University Jena, 07743 Jena, Germany. [9]Abbe Center of Photonics, Friedrich-Schiller-University Jena, 07743 Jena, Germany. [10]Department of Physics and Astronomy, Aarhus University, 8000 Aarhus C, Denmark. [11]Institució Catalana de Recerca i Estudis Avançats (ICREA), Pg. Lluís Companys 23, 08010 Barcelona, Spain.
*These authors contributed equally to this work. †Corresponding author. Email: jens.biegert@icfo.eu

Using this capability, we specifically chose to isolate and examine the dissociation of the C_2H_2 dication ($C_2H_2^{2+} \rightarrow H^+ + C_2H^+$) because it results in a proton H^+ and an ethynyl C_2H^+ moiety. This prototypical dissociation pathway is interesting because it presents one of the fastest expected proton motions and can proceed via two different pathways.

The relevant cuts through the potential energy surface (PES) of C_2H_2 along one C–H direction are shown in Fig. 1A, including states that are relevant for the desired dissociation channel of $C_2H_2^{2+}$ (*30*, *31*) at the present experimental conditions by using a 65-fs (6.3 cycle), 3100-nm pulse (*32*, *33*) with a peak intensity of (65 ± 16) TW/cm^2. The pulse parameters were chosen in order to position the experiment in the sequential double ionization (SDI) regime in which the LIED imaging electron is ejected independently from the first electron in a second tunnel ionization step before scattering off the C_2H_2 dication (supplementary materials). It is known (*26*, *30*, *31*) that the resulting pair of proton H^+ and ethynyl C_2H^+ moiety originates via different possible pathways from the $C_2H_2^{2+}$ dication: (i) The first dissociative excited singlet and triplet states, the $^1\Pi_u$ and the $^3\Pi_u$ states, can be reached through ionization from the σ_g type highest occupied molecular orbital (HOMO)–1 of the neutral ground state ($1\sigma_g^2$, $1\sigma_u^2$, $2\sigma_g^2$, $2\sigma_u^2$, $3\sigma_g^2$, $1\pi_u^2$, $1\pi_u^2$) followed by tunnel ionization from the π_u type HOMO of the excited cationic $^2\Sigma_g^+$ state (*26*, *34*); (ii) the dication possesses a long-lived metastable triplet state [$^3\Sigma_g^-$ lifetime 108 ns (*35*)] and two metastable singlet states ($^1\Sigma_g^+$ and $^1\Delta_g$) that can be reached via sequential tunnel ionization of two π_u electrons. In this case, first one electron tunnels from the HOMO of the neutral ground state ($^1\Sigma_g^+$), populating the singly ionic doublet $^2\Pi_u$ state; then, a second electron tunnels from the HOMO of the singly ionic ground state to populate one of the aforementioned dicationic states. We were interested in the direct dissociation channel that leads to fast proton loss. A simple estimation of the initial speed of the C–H bond elongation, which is based on the curvature of the $^3\Pi_u$ PES, yields an initial elongation velocity of 9 pm/fs from the initial C–H bond length of 1.07 Å in the Frank-Condon region.

To obtain the clearest possible conditions for imaging the direct proton loss channel, and to investigate its dependence on the LIED field, we impulsively aligned the C_2H_2 molecule with an additional 1700-nm, 98-fs pulse focused to a peak intensity of (20 ± 5) TW/cm^2 into the interaction region of the 3100-nm LIED pulse. Having ensured that the 1700-nm pulse did not induce ionization, we could distinguish between the different pathways from a photo-ion/photo-ion coincidence (PIPICO) analysis of our data, which is shown in Fig. 1B (here for perpendicularly oriented C_2H_2). The diagonally sloping line (Fig. 1B, top left to bottom right) shows a very pronounced section [Fig. 1B, top left corner, (i) centered around 0.8 μs/4.1 μs], which corresponds to direct dissociation of the dication from its excited $^1\Pi_u$ and $^3\Pi_u$ states. Section (ii) of this line [Fig. 1B, top left corner 1.0 μs/4.0 μs to bottom right corner 2.6 μs/3.1 μs] is much weaker and is identified with the dication's meta-stable states $^3\Sigma_g^-$, $^1\Delta_g$, and $^1\Sigma_g^+$ (*35*). The proton-ethynyl pairs of the fast deprotonation channel are accompanied by two shallow lines, above and below, respectively associated with reactions involving a ^{13}C atom and a neutral product that is not detected with the reaction microscope: $C_2H_2^{2+} \rightarrow H^+ + C_2^+ + H$. Both of these processes, as well as the slow proton loss channel, occur with a probability two orders of magnitude lower than that for the fast proton loss channel. Nevertheless, we explicitly excluded those channels by isolating the three-dimensional (3D) momentum distribution of the electrons that correspond to the reaction moieties originating from the fast proton loss channel. This permits extraction of structural information only from electrons that rescattered off the H^+ and C_2H^+ fragment pairs from direct dissociation. Additional support to identify population of the fast proton ejection channel (i) stems from measurements of the fragment pair ion yield ($H^+ + C_2H^+$) as a function of delay between alignment and LIED pulse. The results are shown in Fig. 1C and are in excellent agreement with previous work (*36*) in which this temporal dependence was used to identify the two different dication fragmentation channels.

Having identified the direct proton ejection channel (via $^1\Pi_u$ and $^3\Pi_u$), we turned to extracting structural information from its scattered electrons. Our LIED methodology (*20*) permits use of momentum coincidence arguments to associate the scattering electron to only the moieties of the fast proton loss channel. Applying such constraints to the data analysis reduces the event rate by a factor of 83, but the elimination of the general electron scattering background ensures that the resulting momentum map of the electrons bears only structural information

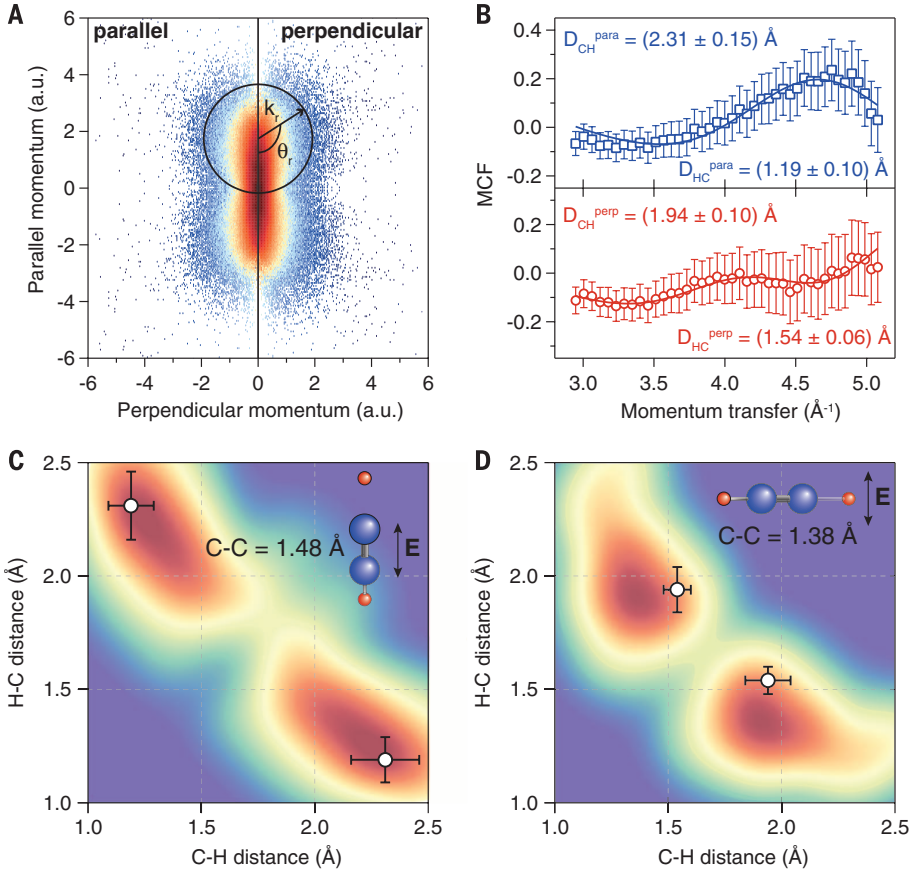

Fig. 2. Measurement of bond distances with LIED. (**A**) The electron momentum distribution in coincidence with the moieties corresponding to the fast proton loss channel. The left half shows data for parallel aligned C_2H_2, and the right half shows data for perpendicularly aligned C_2H_2. (**B**) The MCF for both cases, parallel (top, blue) and perpendicular (bottom, red). Error bars are derived from the experiment based on Poissonian statistics (supplementary materials). (**C** and **D**) Experimental data (white data points with error bars extracted from the MCF fit) overlaid with numerical results (density plot) for cuts through the 3D solution space at the location of its minima. The locations of these cuts correspond to C–C distances of 1.48 Å for the parallel case (C) and 1.38 Å for the perpendicular case (D). (C) shows elongation of one C–H bond to more than twice the equilibrium bond length, corresponding to bond breakage, whereas the other C–H bond is still bound. (D) represents a more symmetric scenario, nearing heterolytic cleavage of one of the two C–H bonds.

of the dissociating C_2H_2 dication (Fig. 2A); the left half of the image shows data for parallel oriented C_2H_2, and the right half of the image shows data for perpendicularly oriented C_2H_2. These momentum maps correspond to the doubly differential electron scattering cross section measured under the influence of the mid-IR LIED field. However, molecular structure is extracted from the field-free molecular differential cross section (mDCS), which is to say that we need to correct for the influence of the mid-IR field. Operating LIED with the 3100-nm pulse in the deep tunneling regime permits application of the semiclassical model (*18*, *37*) in order to determine the vector potential of the LIED field at the time of rescattering for a given electron energy. The vector potential presents the LIED field's influence on the rescattering electron as an offset from zero (field-free) momentum that is simply subtracted from the measurement. The mDCS is then extracted by recording the number of counts along the circumference of a circle whose radius corresponds to the scattering momentum and whose origin is shifted by the vector potential from zero momentum; we show an example in black in Fig. 2A for an electron kinetic energy of 50 eV. Information about the position of the molecule's nuclei is encoded as energy modulations onto the mDCS due to scattering interference. To make these oscillations directly visible, we calculated the molecular contrast factor (MCF), a renormalized quantity, from the mDCS (supplementary materials).

Shown in Fig. 2B are the resulting MCFs for both perpendicularly oriented (Fig. 2B, red circles) and parallel oriented (Fig. 2B, blue squares) C_2H_2. Striking differences are immediately apparent between the MCFs of both orientations, indicating that different structures are observed. The positions of the individual scattering centers, and hence atomic distances, are extracted by calculating MCF patterns for a wide range of possible positions. Comparing the measured MCF with these patterns, we obtained the full 3D solution space (minimum fitted χ^2 value as a function of the C–C distance and two C–H distances) of the instant condition of the molecular wave packet at the time of the electron's return. The solution space is obtained without assumptions such as partially frozen nuclei or linear elongation and includes independent symmetric as well as asymmetric elongation of C–H bonds.

We obtained two different solutions, one for the parallel and one for the perpendicular case, and present 2D cuts through the 3D solution space at those positions: The solution for the parallel case for which we measure a C–C bond length of (1.48 ± 0.11) Å, a value 23% greater than the 1.204 Å equilibrium bond length (*38*) in neutral C_2H_2, is shown in Fig. 2C. Associated C–H distances are (2.31 ± 0.15) Å and (1.19 ± 0.10) Å, corresponding to 118 and 12% elongations, respectively, relative to the 1.06 Å equilibrium value (*38*). This difference, in which one proton has more than doubled its distance to its neighbor, is a clear signature of departure of a proton and hence bond cleavage. The scenario is markedly different for the perpendicular case, in which we measured a C–C bond elongation of 16% from the equilibrium value to (1.38 ± 0.06) Å. The measured C–H distances of (1.94 ± 0.10) Å and (1.54 ± 0.06) Å are shown in Fig. 2D. The more symmetric scenario of C–H bond elongations by 83 and 45% from their equilibrium value is understandable considering that the molecule is aligned perpendicular to the control field when being imaged with the LIED electrons; the molecule is not asymmetrically pulled apart by the strong laser field. This approximates an imaging scenario under quasi–field-free conditions (Fig. 3B). The measured disparity of C–H distances for different alignments provides a means of controlling bond cleavage and proton loss, depending on molecular orientation.

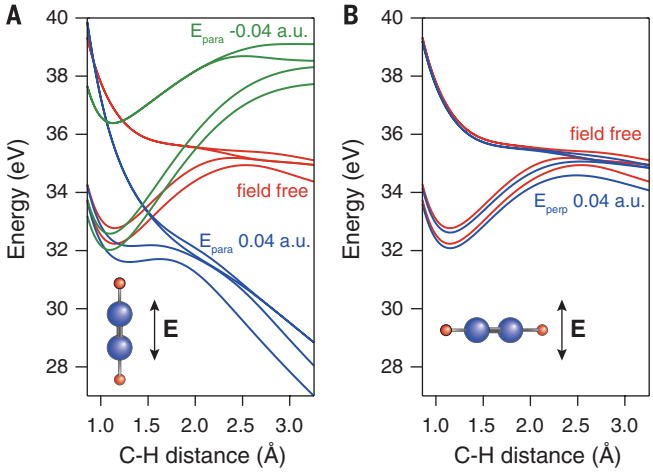

Fig. 3. PES of the C_2H_2 dication with the mid-IR LIED field. (**A** and **B**) The field-free case is shown in red. (A) shows how the PESs Stark-shift when dressed by a mid-IR LIED field aligned with the molecular axis. For one field direction ($E > 0$), all dication PESs are strongly dissociative (blue), whereas for the other field direction ($E < 0$), the PESs present a bound scenario. The trend is exactly reversed for the other C–H bond. (B) shows the doubly degenerate scenario for alignment perpendicular to the mid-IR LIED field, for which we find slight PES shifts but not the dramatic Stark shifts shown in (A).

Next, we sought to explain the difference in imaged structures between the parallel and perpendicularly aligned molecules. We turned to mixed quantum chemistry and semiclassical ab initio molecular dynamics calculations so as to realistically describe the molecular wave packet in the dressing mid-IR field with varying polarization direction as a function of time (supplementary materials). Shown in Fig. 3 is how the PESs of the dication are modified for parallel (Fig. 3A) and perpendicularly oriented (Fig. 3B) molecules in the presence of the LIED field. In Fig. 3, A and B, only the dication's ground states ($^3\Sigma_g^-$ and the near-degenerate singlet states $^1\Delta_g$, $^1\Sigma_g^+$) and the $^1\Pi_u$ and $^3\Pi_u$ excited states are shown, for clarity. For the parallel case (Fig. 3A), we found a stable equilibrium when the LIED field is directed to pull the hydrogen atom toward the carbon atom (Fig. 3A, green). Once the LIED field direction reverses, half a cycle later, all PESs (Fig. 3A, blue) become strongly dissociative, and the C–H bond is broken within 8 fs. Internuclear separation for only one of the two C–H bonds is shown in Fig. 3; the exact opposite scenario occurs at the same time for the other C–H bond (exchange blue with green PESs). In total, during one LIED field cycle (10.3 fs for 3100 nm), one C–H is always broken, whereas the other C–H bond is only elongated. We found excellent agreement with our measured C–C bond length, which is elongated during both half cycles of the LIED field. The calculation yields a C–C bond length of 1.45 Å, which is in excellent agreement with our measured value of (1.48 ± 0.11) Å. The perpendicular case is different because no preferential axis is induced by the LIED field, and hence there are two degenerate cases. Thus, no LIED field direction dependence and only minimal modification of the field-free PESs are exhibited in Fig. 3B. This scenario leads to slower bond dynamics, with eventual breakup. The computed smaller C–C elongation to 1.40 Å agrees with the measured bond length of (1.38 ± 0.06) Å. The simulations show that the C–C bond and the second C–H bond undergo vibration throughout the course of the LIED pulse, yet they stay bound within the temporal range of one optical cycle (10.3 fs).

Because the LIED field does not noticeably distort the PESs in the perpendicular orientation, the C_2H_2 dication behaves like a quasi–field-free electronic system and can be imaged as such. Moreover, the dependence of proton loss dynamics on alignment permits control over the speed and visualization of molecular dissociation.

Having corroborated the dependence of proton loss on alignment, we next linked the measured structures to the times when the snapshots were taken. In our experiment, we analyzed electrons with 50 eV return energy because they yielded the highest number of counts for the largest angular coverage and hence the best scattering momentum transfer. On the basis of the semiclassical model (*18*, *37*), which pertains well for our Keldysh parameter of $\gamma = 0.31$, we can determine the time of return and the backscattering energy for the scattering electron. We only have to consider the long trajectory pathway because of its much higher ionization probability as compared with the short trajectory. We show in Fig. 4A that these electrons have reencountered the target after 9.15 fs (10.3 fs correspond to one optical cycle at 3100 nm) and

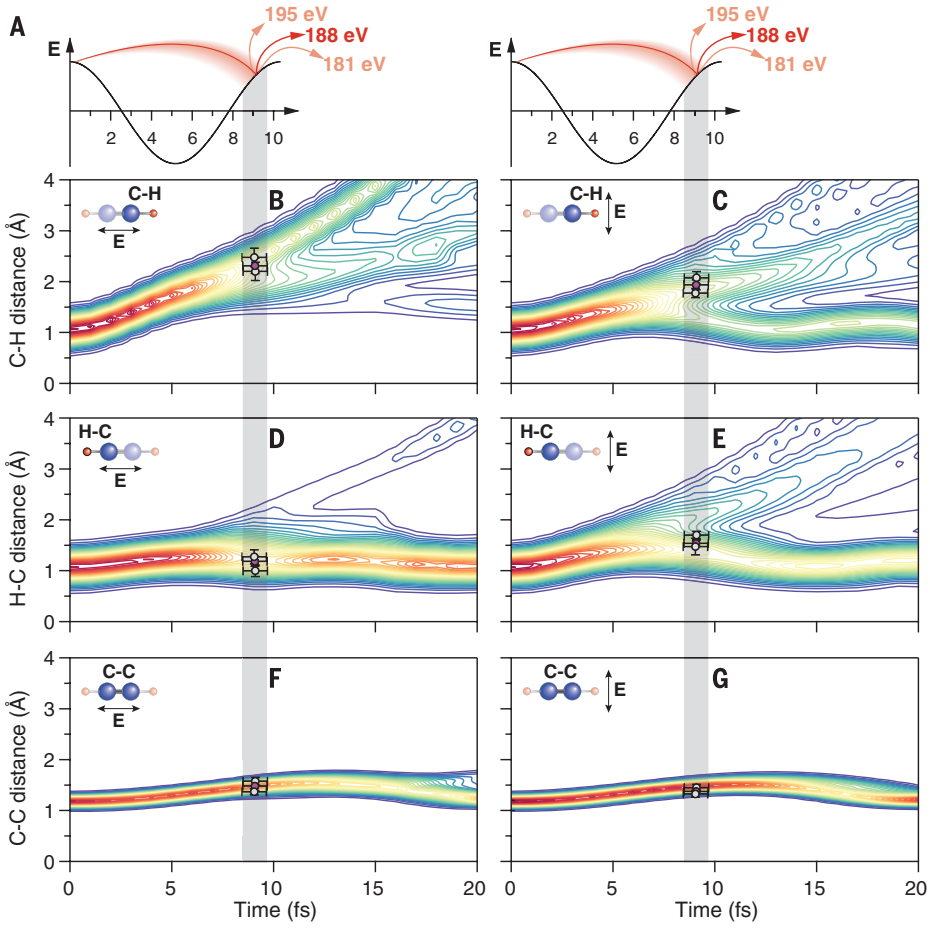

Fig. 4. Temporal dynamics of C_2H_2 resolved for the different bonds and as a function of alignment. (**A**) Temporal range imaged for electron energies ranging up to 195 eV, in accordance with the semiclassical rescattering model. (**B** to **G**) Mixed quantum-classical dynamical calculations are shown below for [(B), (D), and (F)] parallel and [(C), (E), and (G)] perpendicularly aligned C_2H_2. Extracted bond distances from the snapshots taken between 9.1 and 9.2 fs are overlaid onto the calculations and exhibit excellent agreement by being well positioned within the theoretical distribution; the results corresponding to Fig. 2 are shown in pink, and error bars are determined based on the semiclassical rescattering model (supplementary materials). Differences for bond elongation between the [(B) and (D)] parallel and [(C) and (E)] perpendicular cases are clearly resolved.

backscatter with a maximum energy of 188 eV. We additionally analyzed our measurement for two closely neighboring energies of 48 and 52 eV, which correspond to backscattering energies of 181 and 195 eV and for which we achieve high count rates with excellent signal-to-noise ratio. The overall temporal spread is negligible because these three measurements interrogated the molecular structure during a short span between 9.1 and 9.2 fs, as indicated by the vertical gray bars in Fig. 4. The experimental results for the three scattering energies (Fig. 4, circles with error bars) are overlaid with calculated values for all bond distances and for all orientations. The calculated values are based on modeling the experimental conditions with ab initio molecular dynamics simulations that take the modification of the dication states of C_2H_2 by the LIED field fully into account. The simulated evolution of the corresponding probability distribution on the dissociative excited dication state over a time span of 20 fs is shown in Fig. 4, B to G. For parallel orientation (Fig. 4, B, D, and F), the molecule experiences the full LIED field strength along its molecular axis and gets maximally distorted. This scenario corresponds to rapid elongation of one C–H bond (Fig. 4B) and breakage, which is defined at twice its equilibrium distance, after 8 fs. The other C–H bond (Fig. 4D) experiences elongation in the presence of the LIED field, and the C–C bond (Fig. 4F) moves with a period longer than the LIED field's optical cycle. The dynamics change markedly for perpendicular orientation (Fig. 4, C, E, and G), which closely approximates a quasi–field-free imaging scenario (Fig. 3B). We found that the C–C bond undergoes a very similar excursion as that of the parallel case because of the stiffness of the bond. The two C–H bonds, however, show strong probabilities to both oscillate in phase with the LIED field, with some small probability for dissociation. This behavior makes sense, over the shown time range, because there is no preferential direction of the external field that would bias the dynamics of one C–H bond as compared with the other.

The measured snapshots are overlaid (Fig. 4, B, D, and F, circles) with all figures for the parallel case and exhibit excellent agreement with the expected behavior of the molecule. The result from Fig. 2C is indicated by the pink solid circle. Similarly, we show the perpendicular case in Fig. 4, C, E, and G, and found equally excellent agreement with the measurement shown in Fig. 2D.

On the basis of these findings, we can corroborate the full spatiotemporal structure of dicationic C_2H_2 9 fs after ionization. The snapshots of the spatiotemporal structure were taken with an estimated 0.6-fs temporal resolution and are capable of distinguishing the different kinetic behaviors of the molecule when field-ionized parallel or perpendicular to the LIED field. In the parallel case, the snapshots show that one of the hydrocarbon bonds is heterolytically cleaved with the proton 1.24 Å away from its equilibrium position. The perpendicular case snapshots reveal the molecular structure in the quasi–field-free scenario for the dissociative dication.

As a future step, we envision application of our implementation of LIED to triggering and imaging of ultrafast structural transformations over a longer time scale—for example, with two separate pulses as pump and probe, and with molecules with more complex structures. Prospects include structural and spatial isomerization and especially proton tautomerization, a key chemical and biological process that is largely obscured from x-ray scattering techniques.

REFERENCES AND NOTES

1. R. G. Woolley, *J. Mol. Struct. THEOCHEM* **230**, 17–46 (1991).
2. A. H. Zewail, *J. Phys. Chem. A* **104**, 5660–5694 (2000).
3. H. Xu, T. Okino, K. Yamanouchi, *J. Chem. Phys.* **131**, 151102 (2009).
4. J. C. Polanyi, A. H. Zewail, *Acc. Chem. Res.* **28**, 119–132 (1995).
5. M. Chergui, A. H. Zewail, *ChemPhysChem* **10**, 28–43 (2009).
6. M. P. Minitti *et al.*, *Phys. Rev. Lett.* **114**, 255501 (2015).
7. K. Ayyer *et al.*, *Nature* **530**, 202–206 (2016).
8. A. A. Ischenko, S. A. Aseyev, Eds., Time-resolved electron diffraction: For chemistry, biology and materials science, in *Advances in Imaging and Electron Physics* (Elsevier, 2014), vol. 184; www.sciencedirect.com/science/article/pii/B9780128001455210010.
9. P. Zhang, J. Yang, M. Centurion, *New J. Phys.* **16**, 083008 (2014).
10. C. Gerbig, A. Senftleben, S. Morgenstern, C. Sarpe, T. Baumert, *New J. Phys.* **17**, 043050 (2015).
11. S. Manz *et al.*, *Faraday Discuss.* **177**, 467–491 (2015).
12. A. Gliserin, M. Walbran, F. Krausz, P. Baum, *Nat. Commun.* **6**, 8723 (2015).
13. T. Zuo, A. D. Bandrauk, P. B. Corkum, *Chem. Phys. Lett.* **259**, 313–320 (1996).
14. M. Lein, J. P. Marangos, P. L. Knight, *Phys. Rev. A* **66**, 051404 (2002).
15. M. Meckel *et al.*, *Science* **320**, 1478–1482 (2008).
16. C. D. Lin, A.-T. Le, Z. Chen, T. Morishita, R. Lucchese, *J. Phys. At. Mol. Opt. Phys.* **43**, 122001 (2010).
17. C. I. Blaga *et al.*, *Nature* **483**, 194–197 (2012).
18. P. B. Corkum, *Phys. Rev. Lett.* **71**, 1994–1997 (1993).
19. S. Baker *et al.*, *Science* **312**, 424–427 (2006).
20. M. G. Pullen *et al.*, *Nat. Commun.* **6**, 7262 (2015).
21. B. Wolter *et al.*, *Phys. Rev. X* **5**, 021034 (2015).
22. M. G. Pullen *et al.*, *Nat. Commun.* **7**, 11922 (2016).
23. P. M. Kraus *et al.*, *Science* **350**, 790–795 (2015).
24. X. Xie *et al.*, *Phys. Rev. Lett.* **109**, 243001 (2012).
25. A. S. Alnaser *et al.*, *Nat. Commun.* **5**, 3800 (2014).

26. B. Gaire *et al.*, *Phys. Rev. A* **89**, 013403 (2014).
27. H. Ibrahim *et al.*, *Nat. Commun.* **5**, 4422 (2014).
28. G. A. Worth, L. S. Cederbaum, *Annu. Rev. Phys. Chem.* **55**, 127–158 (2004).
29. J. M. Bowman, *Science* **319**, 40–41 (2008).
30. E. M.-L. Ohrendorf, F. Tarantelli, L. S. Cederbaum, *J. Chem. Phys.* **92**, 2984 (1990).
31. R. Thissen *et al.*, *J. Chem. Phys.* **99**, 6590 (1993).
32. J. Biegert, P. K. Bates, O. Chalus, *IEEE J. Sel. Top. Quantum Electron.* **18**, 531–540 (2012).
33. M. Baudisch *et al.*, *J. Opt.* **17**, 094002 (2015).
34. K. Doblhoff-Dier, M. Kitzler, S. Gräfe, *Phys. Rev. A* **94**, 013405 (2016).
35. M. Alagia *et al.*, *J. Chem. Phys.* **136**, 204302 (2012).
36. X. Xie *et al.*, *Phys. Rev. Lett.* **112**, 163003 (2014).
37. J. L. Krause, K. J. Schafer, K. C. Kulander, *Phys. Rev. Lett.* **68**, 3535–3538 (1992).
38. W. M. Haynes, Ed., *CRC Handbook of Chemistry and Physics*, (CRC Press, ed. 94, 2013); www.crcpress.com/CRC-Handbook-of-Chemistry-and-Physics-94th-Edition/Haynes/9781466571143.

ACKNOWLEDGMENTS

We acknowledge financial support from the Spanish Ministry of Economy and Competitiveness (MINECO), through the "Severo Ochoa" Programme for Centres of Excellence in R&D (SEV-2015-0522), grants FIS2014-56774-R and FIS2014-51478-ERC; the Catalan Institució Catalana de Recerca I Estudis Avançats; Agencia de Gestió d'Ajuts Universitaris i de Recerca (AGAUR) with grant SGR 2014-2016; the Fundació Cellex Barcelona; the European Union's Horizon 2020 research and innovation program under LASERLAB-EUROPE (EU-H2020 654148); COST Actions MP1203, XUV/X-ray light and fast ions for ultrafast chemistry (XLIC); the Marie Sklodowska-Curie grant agreement 641272; and the European Research Council through ERC-2013 Advanced Grant 338580. B.W. was supported by AGAUR (FI-DGR 2013–2015). M.G.P. was supported by the ICFONEST+ program, partially funded by the Marie Curie cofunding of Regional, National and International Programs—COFUND (FP7-PEOPLE-2013-COFUND) action of the European Commission. A.-T.L. and C.D.L. are supported by the Chemical Sciences, Geosciences, and Biosciences Division, Office of Basic Energy Sciences, Office of Science, U.S. Department of Energy, under grant DE-FG02-86ER13491. We thank D. Zalvidea, M. Sclafani, and A. Stolow for helpful and inspiring discussions.

SUPPLEMENTARY MATERIALS

www.sciencemag.org/content/354/6310/308/suppl/DC1
Supplementary Text
Figs. S1 to S5
References (*39*–*62*)

13 June 2016; accepted 19 September 2016
10.1126/science.aah3429

METALLURGY

Dynamic creation and evolution of gradient nanostructure in single-crystal metallic microcubes

Ramathasan Thevamaran,[1]* Olawale Lawal,[1] Sadegh Yazdi,[1] Seog-Jin Jeon,[2] Jae-Hwang Lee,[3] Edwin L. Thomas[1]*

We demonstrate the dynamic creation and subsequent static evolution of extreme gradient nanograined structures in initially near–defect-free single-crystal silver microcubes. Extreme nanostructural transformations are imposed by high strain rates, strain gradients, and recrystallization in high-velocity impacts of the microcubes against an impenetrable substrate. We synthesized the silver microcubes in a bottom-up seed-growth process and use an advanced laser-induced projectile impact testing apparatus to selectively launch them at supersonic velocities (~400 meters per second). Our study provides new insights into the fundamental deformation mechanisms and the effects of crystal and sample-shape symmetries resulting from high-velocity impacts. The nanostructural transformations produced in our experiments show promising pathways to developing gradient nanograined metals for engineering applications requiring both high strength and high toughness—for example, in structural components of aircraft and spacecraft.

Creating ultrastrong materials that are also tough enough to resist failure has always been a challenge to material scientists and engineers. In metals, decreasing the grain sizes to the nanoscale has been shown to result in ultrastrong nanocrystalline metals (*1*, *2*). This improvement, however, comes at the cost of increased susceptibility to catastrophic brittle failure as strain localizes in nanocrystalline metals and forms cracks under tensile loading. It has recently been shown (*3*–*6*) that the creation of spatial gradients in grain structure can potentially alleviate the catastrophic failure through progressive ductile behavior under applied uniform tensile stresses. Previous methods for creating a gradient nanograined (GNG) structure require multistep surface mechanical grinding (*3*) or surface mechanical attrition treatment (SMAT) (*5*). Surface mechanical grinding results in a GNG structure with grain sizes increasing from the nanocrystalline (~20 nm) to the coarse-grained (~10 μm) scales from the surface to the interior over a depth of ~0.5 mm, leading to a gradient of grain size ~0.02 (*3*). The SMAT has been shown to produce a GNG structure with grains increasing in size from the ~100-nm nanocrystals to the ~35-μm coarse grains over a depth of ~120 μm, leading to a gradient of grain size ~0.3 (*5*). We demonstrate effective creation of an extreme GNG structure with a single-step, high-velocity-impact process. The high strain rates, pressure, and strain gradients during impact create the GNG structure with a gradient of grain size ~1, where the grain size varies from ~10 to ~500 nm over a distance of ~500 nm. We also show that the high elastic energy stored in the material due to impact triggers a continuous (static) recrystallization process that takes place over the course of weeks at room temperature.

A clear understanding of the fundamental deformation mechanisms in materials exposed to high-velocity impacts and shock compressions is critical to the development of advanced protective technologies for applications in automobile and aircraft crashes (*7*), sport-related collisions (*8*), and body and vehicle armors (*9*). Impact and shock compression are also used for advanced material processing techniques such as shot peening (*10*), laser shock peening (*11*), and explosive welding (*12*). Supersonic velocity microparticle impacts are especially relevant in cold spray technologies (*13*), collision of undetectable small-sized space debris and micrometeorites with spacecraft (*14*), and microparticle impacts on turbine blades (*15*). However, to date, most of the studies on the nano- and micrograins of metals have been limited to quasi-static loading rates of micropillars (*1*, *2*, *16*), due to the challenges in conducting short–time-scale experiments on small-sized samples.

Laser-driven shockwaves have recently been used to probe material responses at small length scales and short time scales (*17*, *18*). Here, we use an advanced laser-induced projectile impact testing (α-LIPIT) apparatus (*19*, *20*) to selectively launch individual single-crystal silver (Ag) microcubes at supersonic velocities (~400 ms^{-1}) and allow them to directly impact a rigid impenetrable target (Fig. 1A). The laser ablation of a gold (Au) thin film produces Au vapor—trapped between the glass substrate and the thin cross-linked polydimethylsiloxane (PDMS) layer—that locally expands the PDMS layer and launches the room-temperature projectile (Ag microcube) at controlled velocities that are proportional to the laser pulse energy (*20*). The PDMS layer also thermally isolates the Ag projectile during laser ablation. This technique allows the sample to deform in an unconstrained manner and enables us to investigate the roles that the intrinsic crystal symmetries and the extrinsic microcube-shape symmetries play on resulting deformations, when the microcube impacts along specific crystal-symmetry directions (Fig. 1, C to E).

[1]Department of Materials Science and NanoEngineering, Rice University, Houston, TX 77005, USA. [2]Department of Polymer Science and Engineering, University of Massachusetts, Amherst, MA 01003, USA. [3]Department of Mechanical and Industrial Engineering, University of Massachusetts, Amherst, MA 01003, USA.
***Corresponding author. Email: thevamaranr@rice.edu (R.T.); elt@rice.edu (E.L.T.)**

Science
AAAS

Ultrafast electron diffraction imaging of bond breaking in di-ionized acetylene

B. Wolter, M. G. Pullen, A.-T. Le, M. Baudisch, K. Doblhoff-Dier, A. Senftleben, M. Hemmer, C. D. Schröter, J. Ullrich, T. Pfeifer, R. Moshammer, S. Gräfe, O. Vendrell, C. D. Lin and J. Biegert

(October 20, 2016)
Science **354** (6310), 308-312. [doi: 10.1126/science.aah3429]

Editor's Summary

Acetylene's scission visualized by selfie

Can molecules take pictures of themselves? That is more or less the principle underlying laser-induced electron diffraction (LIED): A laser field strips an electron from a molecule and then sends it back to report on the structure of the remaining ion. Wolter *et al.* applied this technique to acetylene to track the cleavage of its C–H bond after double ionization (see the Perspective by Ruan). They imaged the full structure of the molecule and also distinguished more rapid dissociative dynamics when it was oriented parallel rather than perpendicular to the LIED field.

Science, this issue p. 308; see also p. 283

Science (print ISSN 0036-8075; online ISSN 1095-9203) is published weekly, except the last week in December, by the American Association for the Advancement of Science, 1200 New York Avenue NW, Washington, DC 20005.